International Journal of Impact Engineering 77 (2015) 1–14

Contents lists available at ScienceDirect

International Journal of Impact Engineering

journal homepage: www.elsevier.com/locate/ijimpeng

Internal-structure-model based simulation research of shielding properties of honeycomb sandwich panel subjected to high-velocity impact☆

Ping Liu [a], Yan Liu [a, b, *], Xiong Zhang [a]

[a] School of Aerospace Engineering, Tsinghua University, Beijing 100084, China
[b] State Key Laboratory of Explosion Science and Technology, Beijing Institute of Technology, Beijing 100081, China

ARTICLE INFO

Article history:
Received 24 April 2014
Received in revised form
31 October 2014
Accepted 3 November 2014
Available online 12 November 2014

Keywords:
High-velocity impact
Honeycomb sandwich panel
Material point method
Internal structure model
Channeling effect

ABSTRACT

Honeycomb sandwich panel has been widely used in aerospace and aeronautic engineering as load-bearing components. Cost-effective shielding structure can also be built based on honeycomb sandwich panel. The shielding properties of honeycomb sandwich panel subjected to high-velocity impact is of great concern to spacecraft design. Three dimensional internal-structure-based simulation research of honeycomb sandwich panels under high-velocity impact is carried out. The point-type internal structure model is constructed, where the impacted area is refined to capture localized deformation and improve the accuracy. The internal structure model is validated by experimental results and empirical formula. Then typical impact processes are simulated to investigate the cutting and channeling effect of the honeycomb core on the projectile. Projectile mass, impact velocity and internal-structure parameters of the honeycomb core are varied to obtain their influences on the channeling effect of the fragmented projectile. The thickness of the honeycomb core influences is found to affect much on the shape of the hole on the rear facesheet. Three empirical equations with respect to impact parameters and internal structure parameters are presented based on numerical results and the dimensional analysis.

1. Introduction

The honeycomb material has been widely applied in engineering fields, such as aerospace engineering and aeronautic engineering, so dynamic responses of honeycomb sandwich panel under different loading conditions are of great interest to scientists and designers. The threat from high-velocity impact to spacecrafts can be very frequent from space debris and meteoroid [1]. As the major load bearing components, honeycomb sandwich panels can also serve as cost-effective shielding structure [2] against impact loading for the functional components inside the spacecraft. The responses of honeycomb panel subjected to high-velocity impact, in addition to the mature researches of statics and low-strain-rate dynamics, should be paid more attention to, since the mechanisms of high-velocity impact and low-velocity impact are quite different. The damage is highly localized during high-velocity impact. Some typical results, such as perforation, spalling, and debris cloud behind the target panel, appear in high-velocity impacts.

The channeling effect of honeycomb core and the ballistic limit of honeycomb panel are often focused, especially in the experimental researches. Sennett and Lathrop [1] found that the honeycomb core has an obvious channeling effect on the debris cloud, implying that the debris cloud after impact spreads a very limited range. The channeling effect can decrease the shielding capability compared to double facesheet structure without honeycomb core. The shielding performance of honeycomb panel for the inside components was also investigated [3–6]. The damage and the signal change in the circuits of the cable bundles behind are emphasized [4–6]. Based on the experimental results, the trajectory and the distribution angles of the debris cloud were expressed as functions of material parameters and impact velocities [7].

☆ Supported by National Natural Science Foundation of China (Grant No. 11102097), the Beijing Higher Education Young Elite Teacher Program (No. YETP0111), National Basic Research Program of China (Grant No. 2010CB832701), and Opening Project of State Key Laboratory of Explosion Science and Technology (Beijing Institute of Technology, and Opening Project Number KFJJ13-4M).

* Corresponding author. School of Aerospace Engineering, Tsinghua University, Beijing 100084, China. Tel./fax: +86 10 62789122.
E-mail address: yan-liu@tsinghua.edu.cn (Y. Liu).

http://dx.doi.org/10.1016/j.ijimpeng.2014.11.004
0734-743X/

In the field of ballistic limit studies, Taylor et al. [8] found that the inclined angles have little effect on the damage of honeycomb panel. Double-layer honeycomb core [2,9] was developed by inserting an extra facesheet in the middle of a honeycomb core. It coincided with the anticipation that the honeycomb panel with double-layer core was found to have better shielding effects than single-layer core [2,9]. The empirical equations for ballistic limits were obtained from experimental results [3,4,10]. Schonberg et al. [11] extrapolated and validated the ballistic limit equation in the range that initial experimental data did not cover. They found that the ballistic limit equation was conservative in predicting the perforation.

Relatively high cost and difficulties in reproducing and capturing results in experiments arouse the interests in numerical methods. The traditional numerical methods have different difficulties in solving high-velocity impact problems due to strong nonlinearity. Mesh-based Lagrangian methods, such as finite element method (FEM), suffer from severely distorted elements which can lead to reduction in time step size and even abrupt computation collapse [12]. Erosion schemes remove the distorted elements, so that the computation can be resumed, but severe accuracy decrease may exist and the total mass is no longer conserved.

The recently fast-developing meshfree particle methods overcome existing difficulties of mesh-based method in large deformation problems. Smoothed particle hydrodynamics (SPH) method, one of meshfree particle methods, was widely used since it was embedded in commercial softwares such as LS-DYNA [13]. Taylor et al. [9] used AUTODYN software to study the performances of different numerical methods. The mesh-based Lagrangian method and SPH method can obtain nearly the same channeling results in 2D simulation. But meshfree models can show more details during the impact process, because no erosion schemes are needed. 3D models for oblique impacts showed that the inclined angles have little effect on the damage of rear facesheet owing to the channeling effect of honeycomb core. Another research by Ryan et al. [14] suggested a method of measuring fragment configuration, which can be used to describe the morphology of the debris cloud quantitatively.

Large computational cost spent on searching neighbor particles sharply increases the computational burden of SPH. Many numerical researches on honeycomb panel with SPH employed only 2D axisymmetric models [9] based on an isotropic assumption of honeycomb panel. When the facesheet is made of anisotropic material or the impact is oblique, however, 3D model for the honeycomb core is demanded [9,14]. An efficient meshfree method, therefore, is highly desired to simulate large-scaled 3D high-velocity impact problems.

Material point method (MPM) is one type of meshfree methods. MPM was proposed by Sulsky et al. [15] as an extension of particle-in-cell method to solid mechanics. Lagrangian points and Eulerian background grids are both employed in MPM computation. Lagrangian points carry all the physical variables, such as the mass, the velocity, the stress and the strain. Lagrangian points describe the deformation and the boundary of the material. The use of Lagrangian points avoids the difficulties in Eulerian method that history variables are not easy to trace and the problems caused by convection terms. Eulerian background grid is used to solve momentum equations and to calculate spatial derivatives, which overcomes the shortcomings in Lagrangian method that large deformation causes element distortion. So MPM owns both the advantages of the Lagrangian and Eulerian methods but overcome their difficulties. MPM can be very efficient for the problems of extremely large deformation and moving discontinuities. On one hand, the critical time step size in MPM is controlled by the background element size, which does not change during the simulation, so the critical time step size will not decrease much even when the material is extremely compressed. On the other hand, no neighbor point search is needed in MPM, so the heavy computational burden of searching process in SPH method is saved. Ma et al. [16] compared MPM and SPH in detail, and they pointed out that the efficiency of MPM is much higher than that of SPH. They also obtained MPM results more accurate than SPH results in impact simulations.

MPM has been successfully applied in the problems of low-velocity impact [17], dynamic fracture [18,19], fluid–structure interaction [20], and high-velocity impact [21–23]. The foam material has randomly sized and distributed voids, which poses great challenges to mesh-based discretization of material internal structure. The reconstruction of material point model for the internal structure of foam material is much easier. Gong et al. [22] constructed the internal structure model of aluminum foam and successfully simulated the high-velocity impact problems based on the material point internal structure model. Liu et al. [23] combined the nano-scale molecular dynamics and the material point method to obtain better parameters for the equation of state under high temperature and high pressure in the hyper-velocity impact process. In our previous work [24], the high-velocity impact of micron particles on the aluminum plate is investigated with material point method. Empirical formulations of cavity dimensions were obtained based on a series of simulations with varying parameters.

In this paper, the dynamical responses of honeycomb sandwich panel under high-velocity impact are studied with MPM-based internal structure model. MPM formulation, the construction of internal structure model, and the material models adopted in the paper are given in Section 2. In Section 3, MPM model is validated by comparing with existing experimental results. The analysis of numerical results of high-velocity impact are discussed in detail in Section 4. Also the influences of the projectile mass and the impact velocity are investigated. The influences of the internal structure parameters of the honeycomb core are studied in Section 5. Three empirical equations are obtained using dimensional analysis in Section 6. Section 7 concludes the whole paper.

2. Model description and simulation method

2.1. The internal structure of the honeycomb material

The honeycomb sandwich panel is usually composed by three parts including the front facesheet, the honeycomb core and the rear facesheet, as shown in Fig. 1. The left part in Fig. 1 is the side view, and the right part shows the in-plane cross section. t_f and t_r

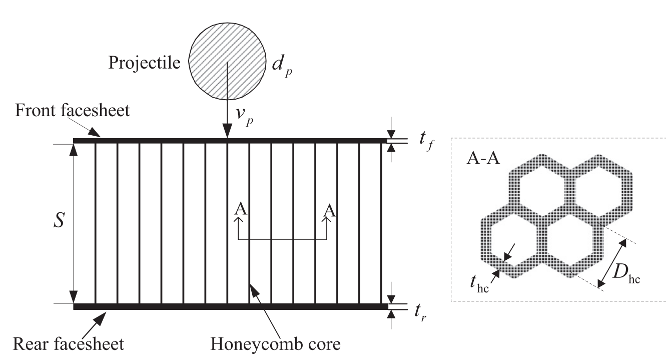

Fig. 1. The structure of the honeycomb panel.

are the thicknesses of the front facesheet and the rear facesheet, respectively. Three structural parameters, t_{hc}, D_{hc} and S, are associated with the honeycomb core. t_{hc} is the thickness of the cell wall, D_{hc} is the diameter of the inscribed circle, and S is the height defined as the distance between two facesheets. One set of structural parameters used in the experiments will be adopted in Section 3 to validate our method. Another model with smaller honeycomb core cell will be calculated in the other sections to investigate the influences of impact and structural parameters.

2.2. Material model

The Johnson–Cook strength model and the Mie–Grüneisen equation of state (EOS) are employed. The strength model is for updating the deviatoric stress s_{ij}, and the EOS is used to update the pressure p. The total stress $\sigma_{ij} = -p\delta_{ij} + s_{ij}$, where δ_{ij} is the Kronecker delta. The yield stress σ_y can be expressed as a function of the equivalent plastic strain ε^p, the strain rate $\dot{\varepsilon}$, and the temperature T in Johnson–Cook strength model [25],

$$\sigma_y = \left(A + B(\varepsilon^p)^n\right)(1 + C\ln\dot{\varepsilon}^*)(1 - T^{*m}) \tag{1}$$

where A, B, n, c, m are material parameters. $\dot{\varepsilon}^* = \dot{\varepsilon}/\dot{\varepsilon}_0$ is the dimensionless equivalent strain rate, and the reference strain rate $\dot{\varepsilon}_0 = 1.0\ \mathrm{s}^{-1}$. $T^* = (T - T_{\mathrm{room}})/(T_{\mathrm{melt}} - T_{\mathrm{room}})$ is the homologous temperature, where T_{room} and T_{melt} are the room temperature and the melting temperature, respectively.

Failure of ductile metals under intensive impact loading can be modeled using different methodologies [26]. Abrupt failure criterion is based on instantaneous failure, that is, when the historical variable reaches a critical value, the material will fail instantaneously. Another type of failure criterion is based on the accumulative damage, that is, when the damage parameter accumulates with deformation to a critical value, the material will fail. Failed material cannot sustain tensile and shearing load but can only afford the pressure.

Both the two types of models are adopted in this paper. One of the first type failure model, the maximum principle stress model, is adopted in order to use material parameters consistent with the references [27,28]. The material fails when the principal tensile stress reaches the criterion value $\sigma_{\max}$. This model can be used to approximately determine the material spall failure.

One of the second type failure model, a sophisticated damage model [29] was developed for the Johnson–Cook strength model, in which the damage is calculated by

$$D = \sum \frac{\Delta\varepsilon^p}{\varepsilon_f^p} \tag{2}$$

where $\Delta\varepsilon^p$ is the increment of equivalent plastic strain in each step, and ε_f^p is the failure strain. When the damage of one material point reaches unity, the material point will fail. The failure strain in the damage model can be calculated as

$$\varepsilon_f^p = [D_1 + D_2 \exp(D_3\sigma^*)][1 + D_4\ln\dot{\varepsilon}^*][1 + D_5 T] \tag{3}$$

where D_1, D_2, D_3, D_4, D_5 are material constants. $\sigma^* = \sigma_m/\overline{\sigma}$ is the stress triaxiality, where σ_m is the mean stress and $\overline{\sigma}$ is the von Mises effective stress.

In high-velocity impact simulation, EOS is always required to update pressure with the volumetric strain, the temperature and the internal energy. Mie–Grüneisen EOS can describe well the mechanical behaviors of metal subjected to impact loading. The pressure in Mie–Grüneisen EOS is calculated as

$$p = p_H\left(1 - \frac{\gamma\mu}{2}\right) + \gamma_0 E_0 \tag{4}$$

where γ is the Grüneisen parameter, which satisfies $\gamma_0\rho_0 = \gamma\rho$, where ρ is the current material density, and γ_0 and ρ_0 are the values at initial state. The volumetric strain $\mu = \rho/\rho_0 - 1$, and E_0 is the initial specific internal energy. p_H is the pressure on the Hugoniot curve,

$$p_H = \begin{cases} \dfrac{\rho_0 c_0 \mu(1+\mu)}{[1-(s-1)\mu]^2} & \text{for } \mu \geq 0 \\ \rho_0 c_0 \mu & \text{for } \mu < 0 \end{cases} \tag{5}$$

where c_0 is the sound speed and s is a material constant.

The Mie–Grüneisen EOS might obtain inappropriate results after the metal melts. The occurrence of melting in high-velocity process strongly depends on the impact velocity. Lee et al. [30] found that the plastic flow can be the major failure factor and melting material is little when the impact velocity is 5 km/s based on their experimental results. All of the impact velocities investigated in this paper are below 5 km/s, so that the use of Mie–-Grüneisen EOS should be reliable.

2.3. Material point method

One set of Lagrangian points, called material points, and an Eulerian background grid are employed in MPM. Lagrangian points carry all the physical variables, such as the mass, the velocity, the stress and the strain. Lagrangian points show the deformation of the material and imply the boundary of the domain. Eulerian background grid serves as the scratch pad to solve momentum equations and to calculate spatial derivatives. Inside each step, the Lagrangian points are bound to the Eulerian grid and they deform together. The traced variables on Lagrangian points are mapped onto the Eulerian grid nodes to establish the momentum equations, which will be solved on grid nodes. After that the point variables are updated by mapping increments of nodal variable back onto the points. The deformed grid is abandoned at the end of every step and the initial undeformed grid will be used in the next step to avoid possible mesh distortion.

If the variables on and before the current time level are known, the flowchart of one MPM step to update variables from the current time level to the next time level is as follows [31,32]. The solution process is also schematically drawn in Fig. 2.

1. A regular Eulerian background grid is used (Fig. 2(a)). The masses and the momenta of material points are mapped onto the new background grid nodes (Fig. 2(b)).
2. The essential boundary conditions are imposed on the grid nodes. If the boundary is fixed in one direction, the momentum of the boundary node in that direction is set to zero.
3. The velocity of the Eulerian grid nodes, and then the increments of the strain tensor and the vorticity tensor of the material points are calculated (Fig. 2(b)). The density of the material point is also updated with the strain increment. After that, new stresses of material points can be obtained by invoking the constitutive model.
4. The internal forces are obtained from the new stresses. If the boundary is fixed in one direction, the boundary nodal forces should be set to zero in that direction.
5. The momenta of grid nodes are updated.
6. The velocities of the material points are updated using interpolation of the nodal accelerations (Fig. 2(c)), and the positions of the material points are updated using interpolation of the nodal velocities (Fig. 2(c)).

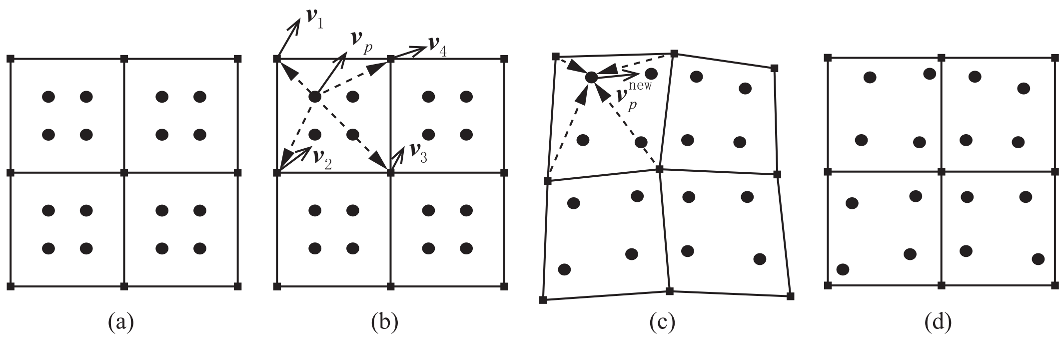

Fig. 2. Schematic flowchart of one time step in material point method.

7. The deformed grid is abandoned and the initial regular background grid will be used in the next step (Fig. 2(d)).

The readers can refer to literatures [15,32,33] for more details and formulations of discretization and implementation of material point method.

The single-valued velocity field is ensured in standard MPM, so a non-slip contact constraint is inherent [32]. The contact algorithm, which is needed for low velocity impact, is not necessary for high-velocity impact, because the contact friction is nearly the same as non-slip friction as the pressure is very large in high-velocity impact. The models with and without contact algorithm were calculated for high-velocity impacts, and results with little deviation were obtained [24].

The critical time step size Δt_{cr} in MPM is controlled by the element size of background grid, which is different from other kinds of meshfree methods, where Δt_{cr} is usually determined by the characteristic length between particles. As a result, Δt_{cr} in MPM can be kept at the same level of its initial value even undergoing extremely large deformation, which is a common process in high-velocity impact. Δt_{cr} in SPH and other meshfree methods, however, can be reduced sharply in large compression process since the particle distances are sharply shortened.

Besides the advantage in critical time step size, MPM possesses another advantage over SPH method that no neighbor point search is needed. Though some techniques such as neighbor list and cell-linked list can be used to increase the efficiency, searching neighbors can even be a serious burden for SPH method especially for large scale computing.

Owing to the above two advantages, MPM can be much more effective than SPH in high-velocity impact simulation. Ma et al. [16] compared MPM and SPH in several aspects. They found that the CPU time per cycle (TPC) of MPM and SPH almost increased linearly with the discretization scale. But the slope of SPH TPC curve is much larger than that of MPM TPC. For the computation of one million points, SPH TPC is more than four times MPM TPC. Ma et al. [16] also compared the performances in Taylor bar impact and hyper-velocity impact problems. MPM configurations are closer to experimental results since some numerical difficulties such as tension stability exist in standard SPH algorithm.

2.4. Discretization of the internal structure of honeycomb core

When space debris impact on the honeycomb panel with very high velocities, the panel may be perforated, and the debris cloud will appear behind the panel. The internal structure walls of the honeycomb core play an important role during the perforation process. On one hand, the cell walls may absorb impact energy and fragment the debris. On the other hand, the cell walls may hinder the debris fragments to expand and result in channeling effect. So it should be necessary to generate three dimensional internal structure for simulating high-velocity impact of honeycomb panel.

The in-plane geometrical structure of honeycomb core is periodic. The cross section of each honeycomb core cell is a regular hexagon, as shown in Fig. 3. Establishing the honeycomb core model can be divided to three steps — to determine the center of one hexagon, to create three edges of one hexagon, and to expand the hexagon cross section periodically. The center position (x_c, y_c) of one hexagon is determined by

$$y_c = \begin{cases} 2n_y \times \dfrac{\sqrt{3}}{2} D_{hc} & \text{for } x_c = 2n_x \times \dfrac{1}{2} D_{hc} \\ (2n_y + 1) \times \dfrac{\sqrt{3}}{2} D_{hc} & \text{for } x_c = (2n_x + 1) \times \dfrac{1}{2} D_{hc} \end{cases} \tag{6}$$

where $n_x = 0,1,2,3...$ and $n_y = 0,1,2,3....$ x_c is the coordinate in the horizontal direction. The symmetry with respect to x-direction and y-direction simplifies the creation of one edge by specularly reflecting one quarter of the edge twice, as shown on the left part of Fig. 3. The ranges of the particles in one quarter, w_t and l_t, have the following relationship

$$l_t = \frac{1}{2\sqrt{3}} (D_{hc} - 2w_t) \tag{7}$$

The remaining edges of each hexagon can be created by rotation after the first one is created owing to cyclic symmetry in every 60°, as shown on the right part of Fig. 3.

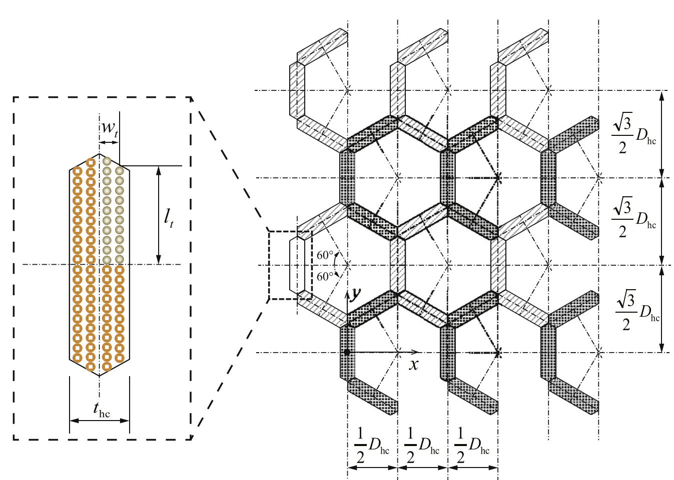

Fig. 3. Schematic process of constructing the material point internal-structure model.

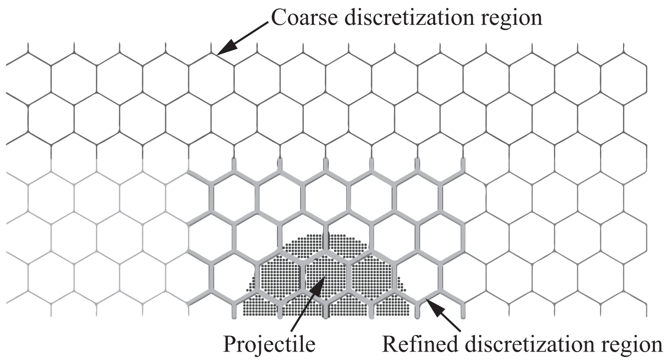

Fig. 4. Locally refined discretization.

The locally refined discretization for the impact region is adopted, as shown in Fig. 4, to capture localized deformation. The refinement in finite element method can be difficult and may result in sharp increase in degrees of freedom and computational cost due to the transition between refined region and coarse region. But the refinement of adding more points in MPM is much simpler. The critical time step size will not change if the background grid is kept the same and no mesh transition exists, so the computational cost will not increase much. The refinement is only used in models where the projectile is larger than one cell. When the projectile is much smaller than one honeycomb core cell, the influence will be almost limited within one cell due to channeling effect. Symmetry of the whole model is invoked to save the computational cost. In Fig. 4, the bold honeycomb region has refined discretization, while the other regions are coarsely discretized.

3. Model validation

Turner et al. [2] performed hyper-velocity impact tests to obtain the ballistic limit of honeycomb sandwich panels. The experimental results of honeycomb panel covered with a thin teflon layer are used to validate our method. In this validation model, $t_r = 0.4$ mm, $t_{hc} = 0.178$ mm, $D_{hc} = 4.76$ mm, and $S = 35$ mm. The teflon layer was suggested to be equivalent to a thin aluminum layer of the thickness 0.1 mm added to the front facesheet [2,9], so that $t_f = 0.5$ mm.

Table 1
Material parameters of validation models.

	Parameter	Al2017 [27,34]	Al2024-T81 [25,28]	Al5052-H19 [26,29,35]
Mie–Grüneisen EOS	c_0 (m/s)	5328	5330	5240
	s	1.34	1.34	1.34
	γ_0	2.0	2.0	2.0
Johnson–Cook strength model	ρ (g/cm^3)	2.79	2.77	2.68
	E (GPa)	73	75	73
	μ	0.33	0.33	0.33
	A (MPa)	265	265	265
	B (MPa)	426	426	426
	n	0.34	0.34	0.34
	C	0.015	0.015	0.015
	m	1.0	1.0	1.0
	T_{melt} (K)	775	775	775
	T_{room} (K)	293	293	293
	c_v (J/kg K)	875	875	875
Failure model	D_1	–	–	0.13
	D_2	–	–	0.13
	D_3	–	–	−1.50
	D_4	–	–	0.011
	D_5	–	–	0
	σ_{max} (MPa)	1580	1500	–

Table 2
Comparison between experimental results [2] and simulation results.

Case number[a]	d_p (mm)	v_p (m/s)	D_r^{exp} [2] (mm)	D_r^{num} (mm)
1 (1-001)	1.0	4690	0.93	NP[b]
2 (1-002)	1.5	4890	5.62	4.90
3 (1-003)	1.2	5270	1.3	2.0
4 (1-004)	0.8	5310	0.48	NP[b]
5 (1-008)	2.0	4570	5.80	5.70
6 (B002)	1.0	1560	NP[b]	NP[b]
7 (B003)	2.0	1770	2.61	3.25

[a] The case number inside parentheses is the experimental case number in Ref. [2].
[b] NP: The projectile does not perforate the rear facesheet of the honeycomb panel.

The facesheets are made of aluminum alloy Al2024-T81, and the material of honeycomb core is aluminum alloy Al5052-H19. The projectile is made of aluminum alloy Al2017. The material parameters are listed in Table 1. Failure model of maximum tensile stress is applied to the projectile and the facesheet material to be consistent with Ref. [27,28], and Johnson–Cook damage model is used for honeycomb material [29].

Results of seven cases are listed in Table 2, and the case numbers used in Ref. [2] are listed as well. D_r^{exp} is the experimental hole diameter of the rear facesheet, which is calculated as the average of the horizontal measurement D_h and the vertical measurement D_v as shown in the left part of Fig. 5(a). The direction of the honeycomb core cell in the experiment is shown in Fig. 5(b). The direction of the honeycomb core cell in the numerical model is different in 30° rotation, but the difference will not affect the results owing to the cyclic symmetry of honeycomb core. So D_h and D_v are measured in 60° and 150° directions for the numerical results (marked as $D_{60°}$ and $D_{150°}$ in the right part of Fig. 5(a)). Numerical simulations successfully predict four perforations (cases 2, 3, 5 and 7) and one no perforation (case 6). Experimental results show a very small hole

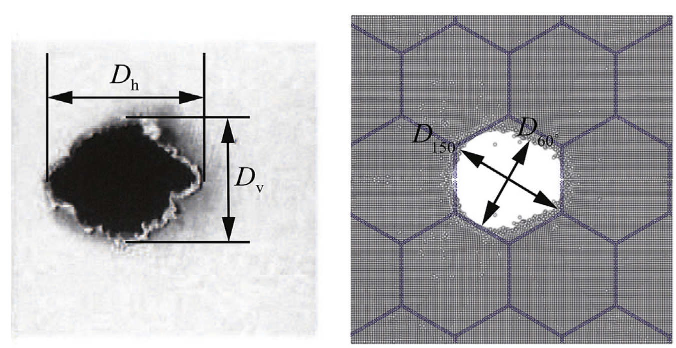

(a) Case 2: Experimental results (left) [9] and MPM results (right)

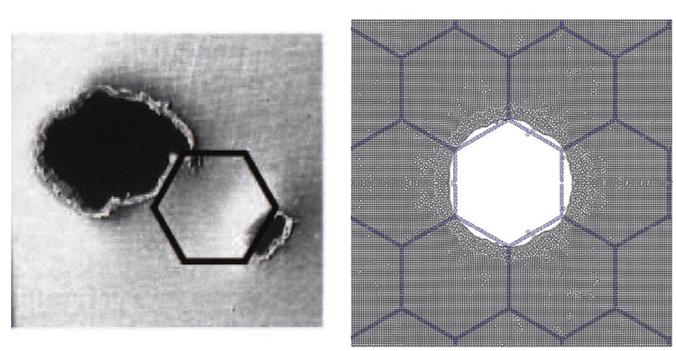

(b) Case 5: Experimental results (left) [9] and MPM results (right)

Fig. 5. Comparison of the hole on the rear facesheet of the validation model.

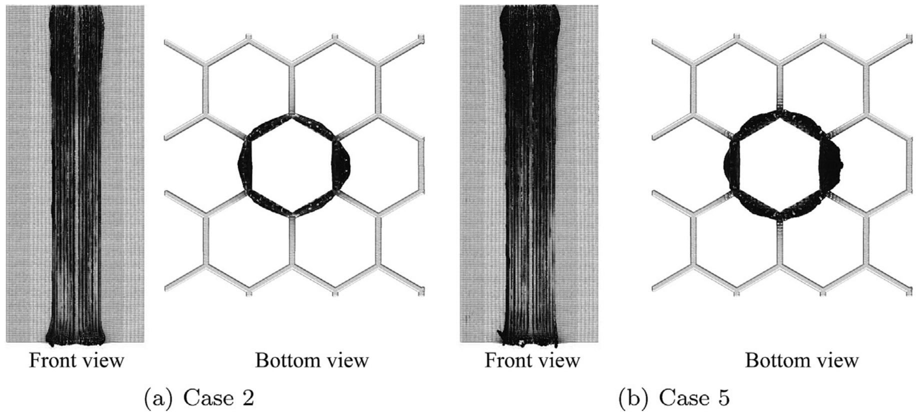

Fig. 6. Damages of the honeycomb core of validation models.

in cases 1 and 4. Though numerical results show no perforation of the rear facesheet, a bulge can be found on the back surface of the rear facesheet.

Fig. 5 also shows the final morphology of the hole on the rear facesheet after impact. Results of case 2 are demonstrated in Fig. 5(a). The experimental hole shows diamond shape rather than circular shape. The numerical result also demonstrates the deviation from circular hole, though the deviation is not as obvious as the experimental result. Results of case 5 are given in Fig. 5(b). The relative difference between numerical and experimental hole diameters is only 1.72%. Both the experimental results and the numerical results show rounder holes on the rear facesheets. Another tiny hole appears in the neighbor cell region, which is not observed in numerical results. Fig. 6 shows damages of the honeycomb core in numerical results. The damaged material point is shown in black. Obvious channeling effect can be seen as the core damage is limited in only one honeycomb cell.

To further validate our simulation, we calculated another three cases that experiments did not cover. The predictions with empirical formula by Schonberg et al. [7], which is concluded based on experimental results from 13 references including Ref. [2], are

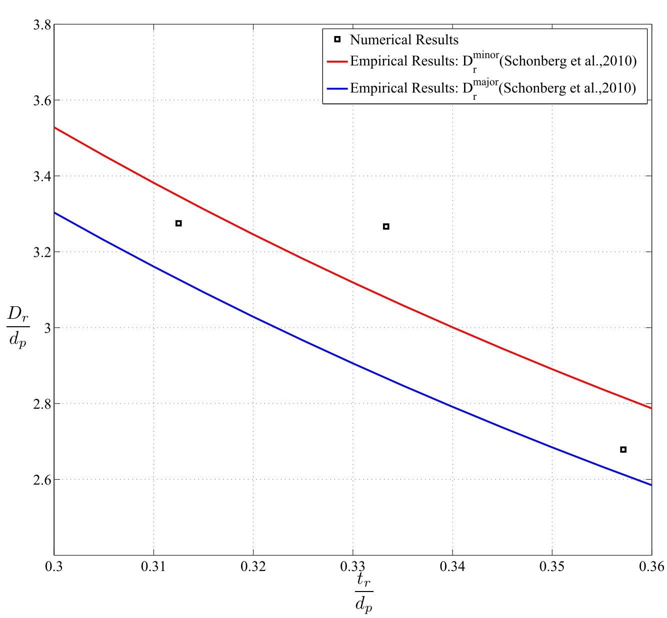

Fig. 7. Dimensionless hole diameters of the rear facesheet comparing with empirical formulation.[7].

compared in Fig. 7. Two MPM results are located between the two empirical curves. The third one is located outside the range but also near the curves. The four perforated cases in Table 2 are also plotted in Fig. 8. Numerical results are more close to the surface of empirical equation than experimental results.

4. Influences of impact parameters

Models with different projectile masses and velocities are established to study the influences of parameters on the mechanical behaviors under high-velocity impact. The emphasis is on the role of the honeycomb cells when the projectile is larger than one cell, so the model parameters are different from those in the validation section. The structure parameters of the honeycomb panel are $t_f = 0.5$ mm, $t_r = 0.5$ mm, $t_{hc} = 0.05$ mm, $D_{hc} = 3.0$ mm, and $S = 14.2$ mm. The information about the projectile and the discretization is given in Table 3, where m_p is the mass of the projectile. The size of the refined area is different for different impact mass so that the refined area size is approximately twice the projectile diameter in the in-plane direction. The model area refers to the whole computational area covered by MPM background cells. The numbers of the material points in each model are also listed in Table 3. Five impact velocities, including 1300 m/s, 2200 m/s, 2900 m/s, 3600 m/s and 4500 m/s, are simulated. It should be noted all the computations are executed on a PC with four CPUs, though the largest model contain more than 28,000,000 points, which is owing to the high efficiency of MPM and the MPM3D code [21,31,36].

Material parameters of computational models are listed in Table 4. The facesheets are made of aluminum alloy Al6061, and the material of honeycomb core is aluminum alloy Al5052. The projectile is also made of aluminum alloy Al6061.

4.1. Analysis of the impact process

Snapshots at different time in a typical process of the honeycomb panel under high-velocity impact are given in Fig. 9, where the projectile mass is 1 g and the impact velocity is 4500 m/s. Material points with different colors refer to different components in Fig. 9(a). Black material points represent damaged materials of honeycomb core in Fig. 9(b)–(i). At the beginning of the impact, the front facesheet is perforated similar to the impact process of a single thin plate. The projectile is not fragmented since the thickness of the front facesheet is much smaller than the diameter of the projectile. The projectile and the failed target material move downward together into the honeycomb core. The walls of

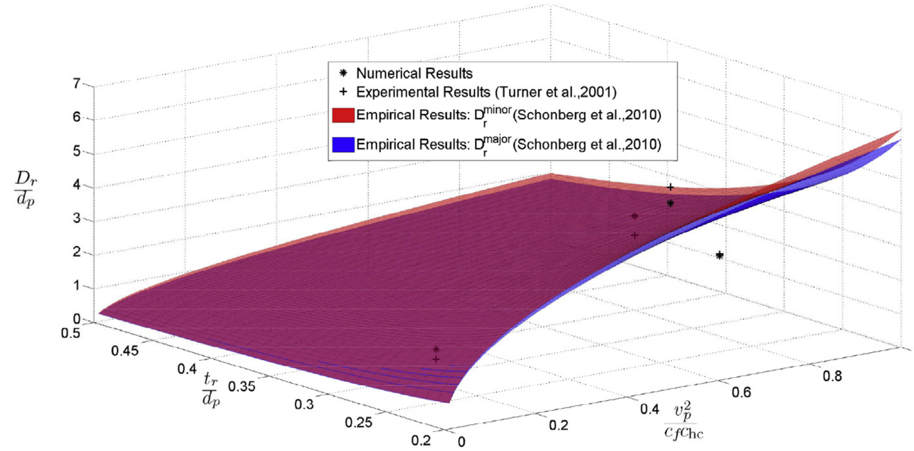

Fig. 8. Dimensionless hole diameters of the rear facesheet comparing with experimental results [2] and empirical formulation.[7].

honeycomb core cut the unfailed projectile to several parts. The channeling effect on the fragments and the failed material of the front facesheet can be observed. The fragmented debris are confined in a few honeycomb cells surrounding the impact point. The honeycomb core cells right under the projectile also fail under such intensive loading. The fragments, including the fragmented projectile, the failed front facesheet material and the failed honeycomb core material, continue moving until reaching, striking on and perforating the rear facesheet. Finally a debris cloud is formed at the back of the panel.

For the other projectiles with different masses and velocities, the impact processes are similar. Differences lie in the sizes of failed region and the channeling effects. Fig. 10 shows the configurations of $v_p = 2200$ m/s at $t = 6\mu$ s and $t = 7\mu$ s, and of $v_p = 4500$ m/s at $t = 3\mu$ s. The projectile mass $m_p = 1$ g. The observation times are chosen so that the configurations of different velocities are at nearly the same stage. The channeling effect for $v_p = 4500$ m/s is less obvious. The second nearest neighbor cells have been penetrated and the debris fragments are still expanding. While for the case $v_p = 2200$ m/s, most of the fragments are confined inside the neighbor cells, though the walls of the second nearest neighbor cells are broken. The damage of the cell walls are plotted for $m_p = 2$ g and $v_p = 1300$ m/s, 2900 m/s and 4500 m/s in Fig. 11. A nearly straight channel can be found in the plot of the lowest velocity. Cone-shaped channel is observed when $v_p = 2900$ m/s, but the taper is still small. A more obvious cone-shaped channel appears for $v_p = 4500$ m/s. The above results indicate that the shielding capability can be better for higher velocities since the impacted debris spread much larger range.

Fig. 12 compares the performances of honeycomb panel for different projectile mass when $v_p = 4500$ m/s. Larger projectile can destroy larger region, so the channel taper is a little larger for large projectile, but the influence of the mass on the channeling effect and the shielding capability is not as obvious as the influence of impact velocity.

Table 3
Parameters of computational models.

m_p (g)	d_p (mm)	Refined area (mm^2)	Model area (mm^2)	Total number of material points
1	8.81	18 × 9	36 × 18	6,272,164
2	11.10	24 × 12	42 × 21	7,508,928
5	15.07	30 × 15	60 × 30	10,903,472
10	18.99	36 × 18	72 × 36	17,205,264
20	23.92	48 × 24	90 × 45	28,456,320

4.2. Analysis of hole morphology

A cone-shaped hole is usually formed in the panel after perforation, that is, the hole diameter of the rear facesheet is larger than that of the front facesheet. The debris generated by the impact on the front facesheet will spread a much wider range if there was no honeycomb core [7]. As a result, the hole on the rear facesheet is usually larger than that on the front facesheet though the channeling effect exists.

Typical final morphology and the measurement method of hole dimensions are shown in Fig. 13. The hole on the front facesheet is close to a circle, while the shape of the hole on the rear facesheet deviates from a circle because of the cutting effect of the honeycomb core on the projectile. D_h and D_v are the horizontally and vertically measured diameters, respectively. The equivalence diameter of the hole on the front facesheet is determined by averaging D_h and D_v,

$$D_f = \frac{D_h + D_v}{2} \tag{8}$$

Table 4
Material parameters of computational models.

Material model	Parameter	Al6061 [37]	Al5052 [26,29,35]
Mie–Grüneisen EOS	c_0 (m/s)	5350	5350
	s	1.34	1.34
	γ_0	2.0	2.0
Johnson–Cook strength model	ρ (g/cm^3)	2.77	2.68
	E (GPa)	75	73
	μ	0.33	0.33
	A (MPa)	265	265
	B (MPa)	426	426
	n	0.34	0.34
	C	0.015	0.015
	m	1.0	1.0
	T_{melt} (K)	775	775
	T_{room} (K)	293	293
	c_v (J/kg K)	875	875
Failure model	D_1	−0.77	0.13
	D_2	1.45	0.13
	D_3	−0.47	−1.50
	D_4	0.0	0.011
	D_5	1.6	0

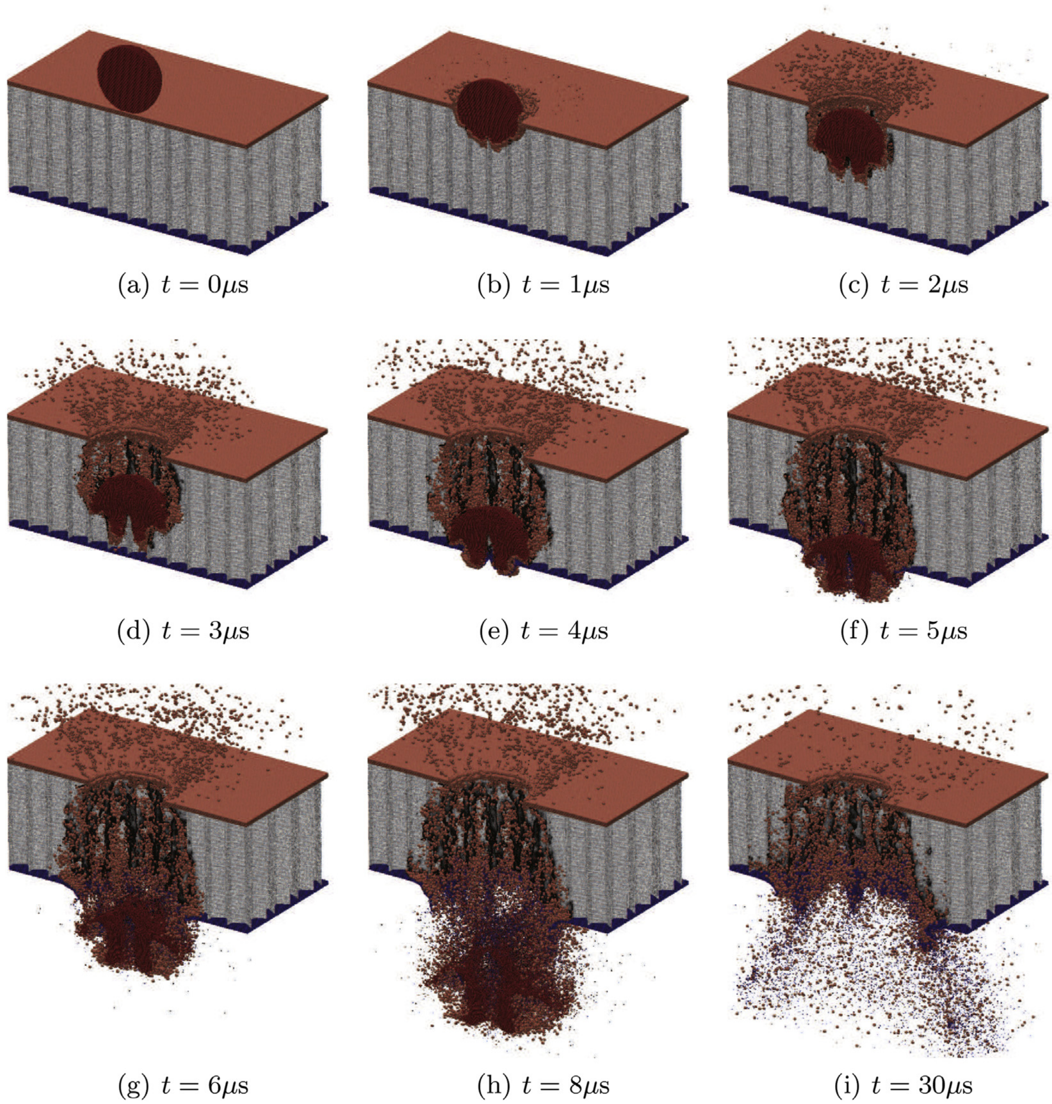

Fig. 9. High-velocity impact process of the honeycomb sandwich panel. $m_p = 1$ g and $v_p = 4500$ m/s.

Determining D_h and D_v of the hole on the rear facesheet is more complicated due to the anisotropy and the cutting effect of the honeycomb core, so the dimensions in several directions are measured and averaged to calculate D_h and D_v. As the honeycomb core has cyclic symmetry in every 60°, D_h is averaged with measured values in the directions at the angles of every 60° starting from the horizontal line. D_v is also averaged by the dimensions in the directions at multiples of 60° from the vertical line.

$$D_\mathrm{h} = \frac{D_{0^\circ} + 2D_{60^\circ} + 2D_{120^\circ} + D_{180^\circ}}{6} \tag{9}$$

$$D_\mathrm{v} = \frac{D_{30^\circ} + D_{90^\circ} + D_{150^\circ}}{3} \tag{10}$$

D_{0°, D_{30°, D_{60°, D_{90°, D_{120°, D_{150° and D_{180° are the measurements at different angles with respect to the horizontal direction as shown

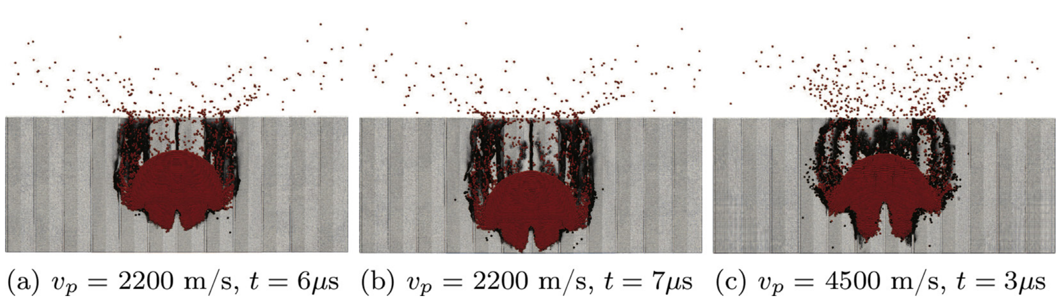

Fig. 10. Debris fragmentation and configurations of honeycomb sandwich panel for different velocities. $m_p = 1$ g.

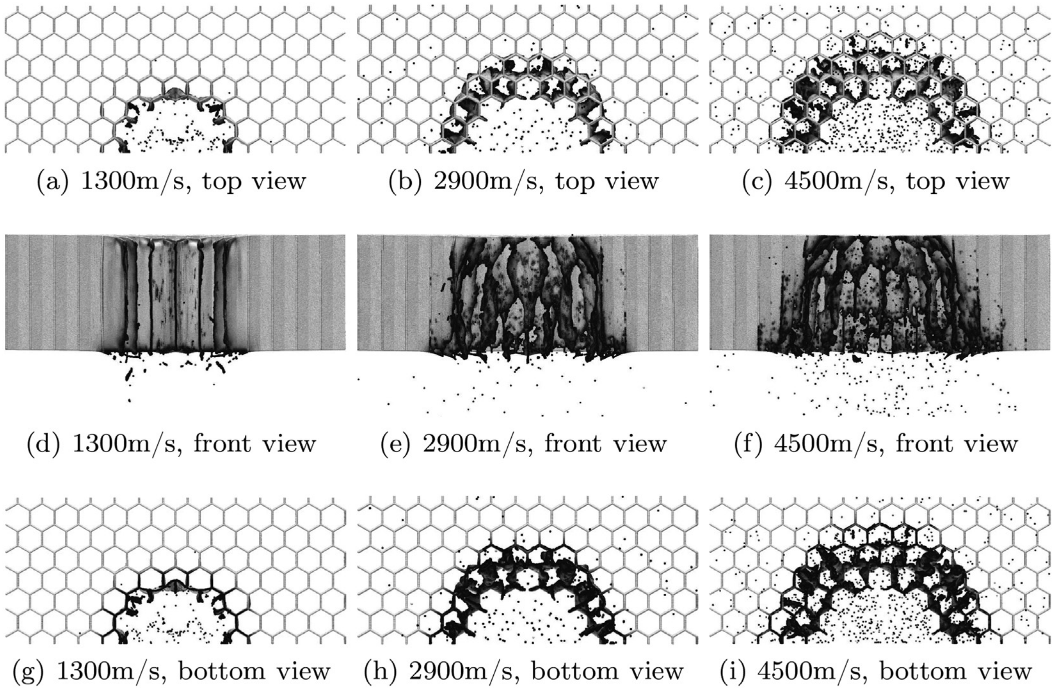

Fig. 11. Final morphologies of honeycomb core for different velocities. $m_p = 2$ g.

in Fig. 13. The coefficient two for D_{60° and D_{120° in equation (9) is added because the symmetry with respect to the horizontal line is invoked. The equivalent diameter of the hole on the rear facesheet is then calculated by averaging D_h and D_v.

4.2.1. The eccentricity of the holes

To describe the deviation of the hole shape from a circle, the eccentricity of the hole is defined as.

$$e = \frac{D_\mathrm{h}}{D_\mathrm{v}} \tag{11}$$

When $|e| \to 1$, the hole approaches to a circle. e_f and e_r represent respectively the eccentricities of the holes on the front and the rear facehseets. The values of e_f are very close to one despite the velocity and the projectile mass, which can be expected from Fig. 13 that the hole on the front facesheet is very smoothed and regular. Most of e_r are more than one, but the largest difference between e_r and unity is less than 5%, which means that the holes on the rear facesheet do not deviate much from circles. So an equivalent circle can be assumed for the above models to describe the holes on both the facesheets.

4.2.2. The hole on the front facesheet

Hole diameters of the front facesheets (D_f) are given in Table 5. D_f increases as the projectile mass and the impact velocity increase. But D_f mainly depends on the projectile diameters, and impact velocity has relatively much smaller influence.

The problem of a single aluminum plate under hyper-velocity impact is also simulated. The thickness of the plate is same as that of the front facesheet. The hole diameters are found to be nearly the same as the hole diameters of the front facesheet. D_f is also compared with the results of impact on a single plate from the reference, as shown in Fig. 14. The curve represents the fitting function of experimental results [38]. MPM results show good agreement with experimental results. In conclusion, the hole diameter on the front facesheet is mainly determined by the projectile and the front facesheet, while the honeycomb core and the rear facesheet has little influence. This is because the impact process is very transient and localized, and the strengthened effect of the honeycomb core cannot be reflected.

4.2.3. The hole on the rear facesheet

Table 6 shows hole diameters of the rear facesheets (D_r). D_r also increases with increasing the projectile mass and the impact velocity. But D_r shows much more dependence on the velocity, which is very different from D_f.

The variation of D_f and D_r with respect to impact energy are plotted in Fig. 15. Fitted curve of D_f and D_r in power functions are also plotted in Fig. 15. The data of D_r can be well fitted with power function with respect to the impact energy, and the fitting goodness is 0.9583. The fitting goodness of D_f is only 0.6766, because they are

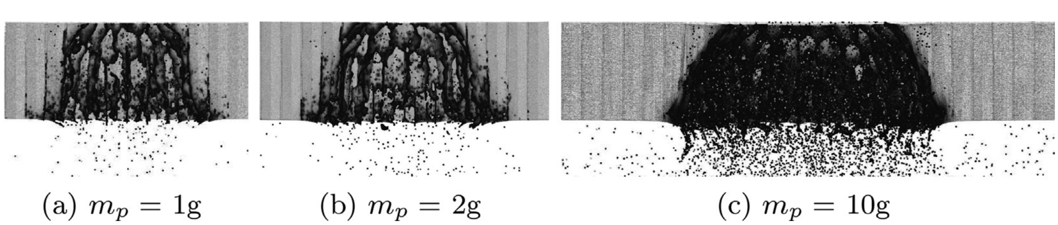

Fig. 12. Final morphologies of honeycomb core for different projectile masses. $v_p = 4500$ m/s.

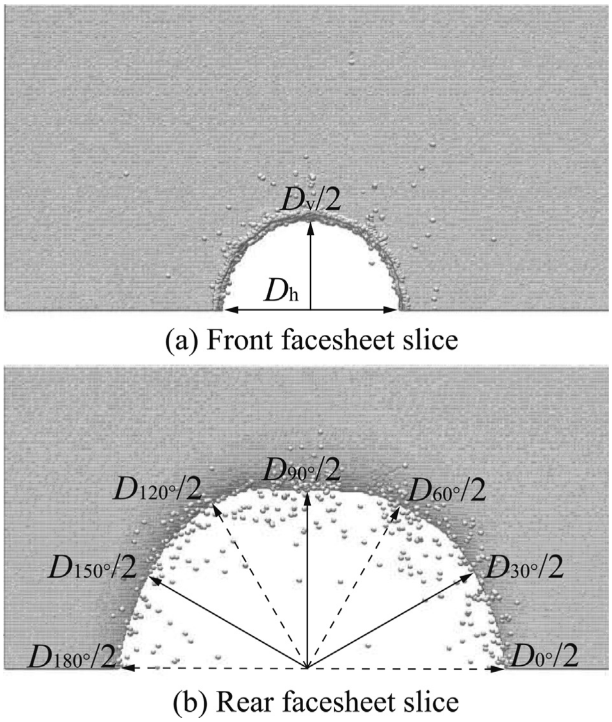

Fig. 13. Top views of the front and the rear facesheets after impact and the measurement method of hole dimensions. $m_p = 1$ g and $v_p = 4500$ m/s.

affected greatly by the projectile size. The velocity-influenced diameter is then defined as the hole diameter minus the projectile diameter ($D_f - d_p$), which has a better power function relationship with impact energy, and the fitting goodness is 0.7611.

4.2.4. The impacted channel in the honeycomb core

The taper of the impact channel in the honeycomb core is calculated as.

$$t = \frac{D_r - D_f}{S} \tag{12}$$

which can be used to describe the channeling effect of the honeycomb core. Larger taper implies less channeling effect. As discussed in Section 4.1, the taper is much influenced by the impact velocity. Larger projectile also brings larger taper. The taper is fitted with a power function with respect to the impact energy in Fig. 16. The fitting goodness is 0.8060. The channeling effect is more obvious when the impact energy is lower. This is because the projectile has less energy to destroy the cell walls of the honeycomb core, so the projectile fragments are mainly confined in a small area. When the impact energy is high, the projectile has enough energy to penetrate the cell walls to spread larger range.

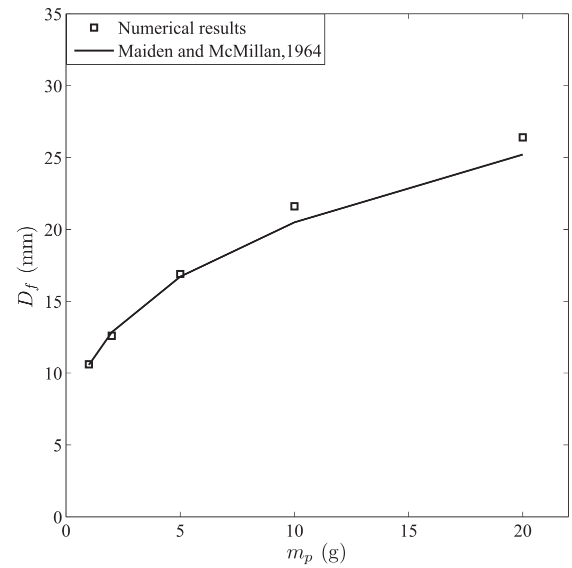

Fig. 14. Comparison of hole diameters of the front facesheet with experimental work of impact on single plate [38]. $v_p = 4500$ m/s.

5. Influences of internal structure parameters

The internal structure parameters of the honeycomb core are expected to have an essential effect on the final morphology and the shielding capability of honeycomb sandwich panel. The parameters D_{hc}, S, and t_{hc} are varied to observe their influences. The projectile mass is fixed as 1 g and the projectile velocities are 2200 m/s and 4500 m/s. The measured hole sizes and tapers are listed in Table 7. The reference results, which are the results of the structure analyzed in Section 4, are listed in the first and the third rows for comparison.

The changes of D_f are very small, which are less than 2% when $v_p = 2200$ m/s and less than 3% when $v_p = 4500$ m/s for the computed structure parameters. This can be understood that the core has little influence on the perforation process of the front facesheet as discussed in Section 4.2.2. D_r are influenced much by internal structure parameters. D_r has an increasing trend when D_{hc} increases and t_{hc} decreases. S also has important influences on D_r when it is small. The eccentricity e_r does not change much for different internal structure parameters. The shape of the hole differs much especially when t_{hc} varies. The final morphologies of the hole on the rear facesheet for different t_{hc} are given in Fig. 17, where the figures in the first and the third rows are 3D views of the rear facesheet and those in the second and the fourth rows are the top views. The anisotropic effect of the honeycomb core becomes more obvious when t_{hc} increases, that is, the hole is no longer a smoothed circle with t_{hc} increasing.

The tapers shown in Table 7 have obvious dependence on all the internal structure parameters. The taper increases when D_{hc}

Table 5
Hole diameters of the front facesheet (D_f, in millimeters).

m_p (g)	v_p (m/s)					d_p (mm)
	1300	2200	2900	3600	4500	
1	9.27	10.00	10.07	10.13	10.60	8.81
2	11.60	12.07	12.60	12.53	12.60	11.10
5	16.20	16.47	16.80	17.00	16.93	15.06
10	20.07	20.27	20.47	21.07	21.60	18.99
20	25.13	25.53	25.80	25.87	26.40	23.92

Table 6
Holes diameters of the rear facesheet (D_r, in millimeters).

m_p (g)	v_p (m/s)					d_p (mm)
	1300	2200	2900	3600	4500	
1	13.70	17.63	19.42	21.57	22.63	8.81
2	16.97	20.78	22.20	23.63	25.77	11.10
5	21.90	26.72	30.37	32.20	33.98	15.06
10	27.03	31.52	34.55	37.42	39.22	18.99
20	31.87	37.00	40.50	43.40	45.60	23.92

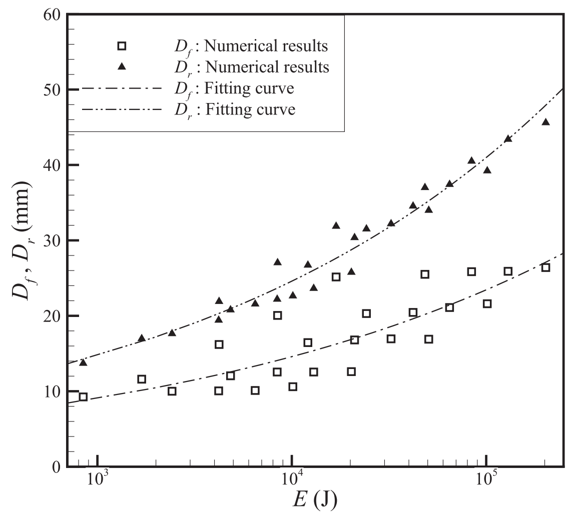

Fig. 15. D_f and D_r versus impact energy.

increases, S decreases and t_{hc} decreases. Larger taper stands for less channeling effect. When D_{hc} decreases, the energy required for the projectile fragments to spread will increase because they need to destroy more cell walls, so that the channeling effect will increase. The channeling effect will also become more obvious if t_{hc} increases because the fragments have to perforate thicker cell walls. Increasing S implies that the debris have more chances to impact on the cell wall, so the channeling effect also increases.

6. Dimensional analysis

The variables included in the dimensional analysis model [7] are listed as follows.

$$\text{Projectile}: \rho_p, c_p, v_p, d_p$$

$$\text{Front facesheet}: D_f, \rho_f, c_f, t_f$$

$$\text{Rear facesheet}: D_r, \rho_r, c_r, t_r$$

$$\text{Honeycomb core}: \rho_{hc}, c_{hc}, D_{hc}, t_{hc}, S$$

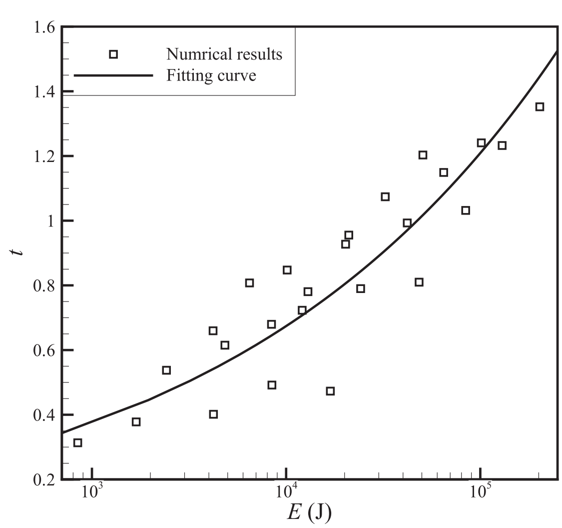

Fig. 16. Impacted channel taper of honeycomb core versus impact energy.

where ρ and c are the density and the sound speed, respectively. The subscript p, f, r and hc denote respectively the projectile, the front facesheet, the rear facesheet and the honeycomb core. The meanings of other variables are described in the previous sections.

For the front facesheet, the velocity-influenced hole diameter $(D_f - d_p)$ is mostly affected by the parameters of the projectile and the front facesheet, as discussed in Section 4.2.2. So eight variables associated with the projectile and the front facesheet are considered in the dimensional analysis model. Five non-dimensional variables are required according to π-theorem. The relationship is given as follows,

$$\frac{D_f - d_p}{d_p} = f\left(\frac{v_p}{c_f}, \frac{t_f}{d_p}, \frac{\rho_f}{\rho_p}, \frac{c_f}{c_p}\right) \tag{13}$$

where $\rho_f/\rho_p = 1$, $c_f/c_p = 1$ in the current problem, so that equation (13) degenerates to the following form

$$\frac{D_f - d_p}{d_p} = f\left(\frac{v_p}{c_f}, \frac{t_f}{d_p}\right) \tag{14}$$

A power function is assumed for fitting the results. Multiple linear regression using least squares is adopted here to obtain the coefficients. The significance level $\alpha = 0.05$. The fitted equation is

$$\frac{D_f - d_p}{d_p} = 1.462\left(\frac{v_p}{c_f}\right)^{0.7658}\left(\frac{t_f}{d_p}\right)^{0.6352} \tag{15}$$

where the fitting goodness $R^2 = 0.8794$. The function surface is shown in Fig. 18, where the symbols represent the numerical results, and the meshed surface is equation (15).

For the rear facesheet, the hole diameters are mainly affected by the parameters of the projectile, the honeycomb core, and the rear facesheet [7]. Because the thickness of the rear facesheet t_r is not changed in all the simulations, twelve parameters need to be considered, and nine non-dimensional variables are required according to the π-theorem. The assumed function is as follows,

Table 7
Results for different internal structure parameters.

v_p (m/s)	Parameter	Value (mm)	D_f (mm)	D_r (mm)	e_r	t
2200 (reference results)	D_{hc}	3.0[a]	10.07	17.63	1.03	0.54
	S	14.2[a]				
	t_{hc}	0.05[a]				
2200	D_{hc}	1.5	9.87	15.47	1.10	0.39
		4.5	10.00	17.93	1.03	0.56
	S	4.5	9.95	14.51	1.00	1.01
		5.4	10.02	15.10	0.99	0.94
		7.1	10.07	15.37	1.03	0.74
		21.30	10.00	16.87	1.08	0.32
	t_{hc}	0.1	9.93	16.00	1.03	0.43
		0.15	9.93	16.67	0.98	0.47
4500 (reference results)	D_{hc}	3.0[a]	10.60	22.63	1.03	0.85
	S	14.2[a]				
	t_{hc}	0.05[a]				
4500	D_{hc}	1.5	10.73	20.60	1.01	0.69
		4.5	10.67	24.00	1.06	0.94
	S	4.5	10.92	16.60	0.99	1.28
		5.4	10.78	18.60	1.00	1.44
		7.1	10.63	19.73	1.04	1.28
		21.30	10.73	23.60	1.06	0.60
	t_{hc}	0.1	10.87	21.73	1.05	0.76
		0.15	10.80	19.20	1.00	0.59

[a] Values for the structure analyzed in Section 4.

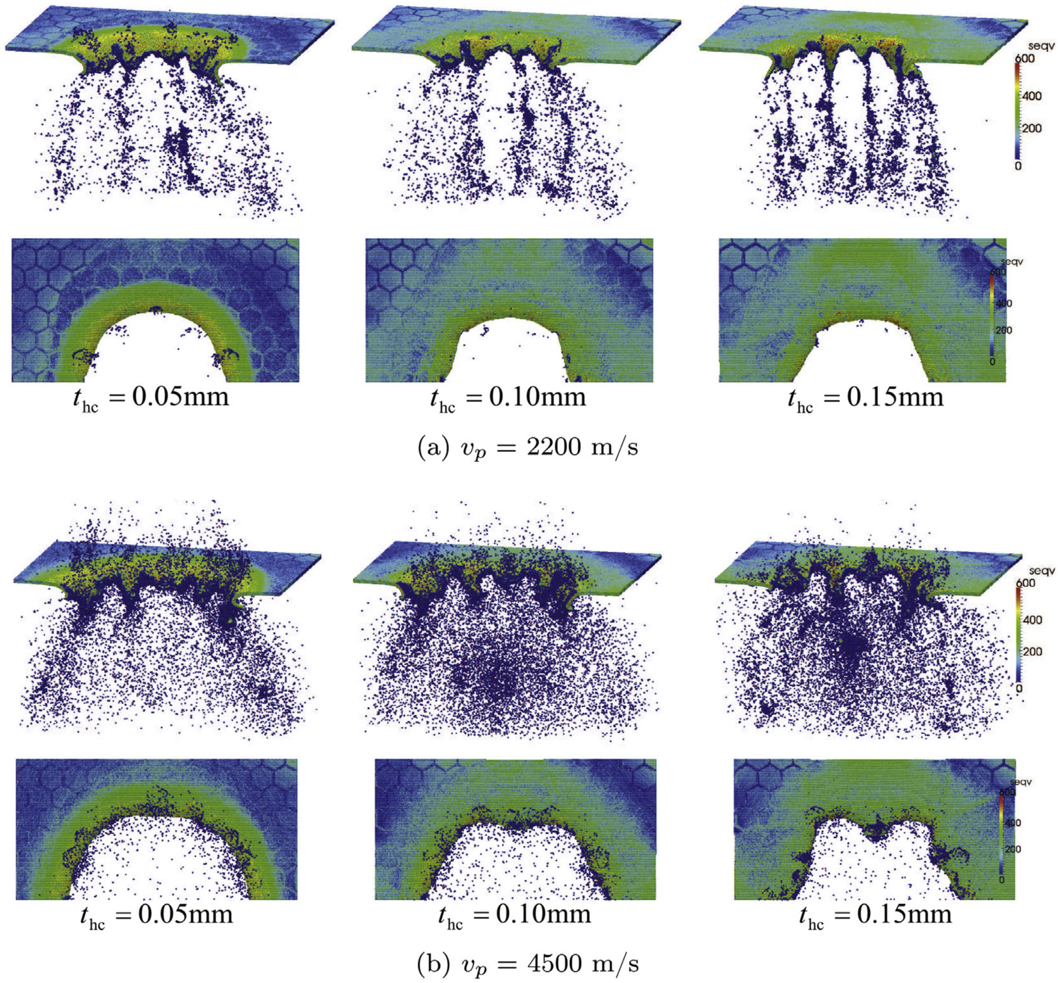

Fig. 17. The morphologies of the holes on the rear facesheet for different t_{hc}.

$$\frac{D_r}{d_p} = f\left(\frac{v_p^2}{c_r c_{hc}}, \frac{t_{hc}}{d_p}, \frac{t_{hc}}{D_{hc}}, \frac{t_{hc}D_{hc}}{S^2}, \frac{\rho_r}{\rho_p}, \frac{\rho_{hc}}{\rho_p}, \frac{c_r}{c_p}, \frac{c_{hc}}{c_p}\right) \tag{16}$$

Similar to equations (14) and (16) has the following degeneration form,

$$\frac{D_r}{d_p} = f\left(\frac{v_p^2}{c_r c_{hc}}, \frac{t_{hc}}{d_p}, \frac{t_{hc}}{D_{hc}}, \frac{t_{hc}D_{hc}}{S^2}\right) \tag{17}$$

where $\rho_r/\rho_p = 1$, $\rho_{hc}/\rho_p = 1$, $c_r/c_p = 1$, and $c_{hc}/c_p = 1$ has been invoked. Equation (17) is fitted with power function as

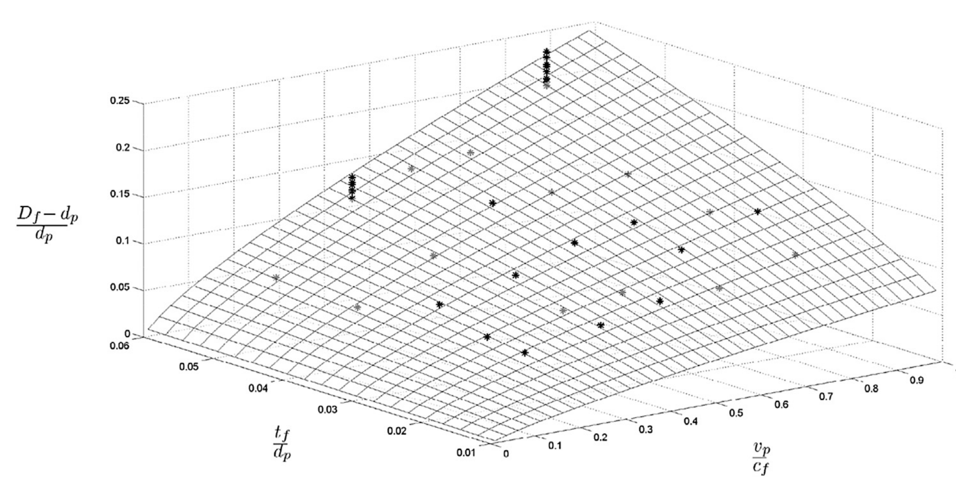

Fig. 18. The fitted surface of non-dimensional velocity-influenced diameter of the hole on the front facesheet.

$$\frac{D_r}{d_p}=1.901\left(\frac{v_p^2}{c_r c_{hc}}\right)^{0.1695}\left(\frac{t_{hc}}{d_p}\right)^{0.2245}\left(\frac{t_{hc}}{D_{hc}}\right)^{-0.2150}\left(\frac{t_{hc}D_{hc}}{S^2}\right)^{-0.0850} \tag{18}$$

with fitting goodness $R^2 = 0.9604$.

For the taper of the channel in the honeycomb core, there are thirteen variables, of whom ten non-dimensional parameters are required,

$$t = f\left(\frac{v_p^2}{c_r c_{hc}}, \frac{t_{hc}}{d_p}, \frac{t_{hc}}{D_{hc}}, \frac{t_{hc}D_{hc}}{S^2}, \frac{\rho_f}{\rho_p}, \frac{\rho_r}{\rho_p}, \frac{\rho_{hc}}{\rho_p}, \frac{c_f}{c_p}, \frac{c_r}{c_p}, \frac{c_{hc}}{c_p}\right) \tag{19}$$

The degeneration form is

$$t = f\left(\frac{v_p^2}{c_r c_{hc}}, \frac{t_{hc}}{d_p}, \frac{t_{hc}}{D_{hc}}, \frac{t_{hc}D_{hc}}{S^2}\right) \tag{20}$$

and the final form can be obtained as

$$t = 0.5865\left(\frac{v_p^2}{c_r c_{hc}}\right)^{0.3751}\left(\frac{t_{hc}}{d_p}\right)^{-0.5238}\left(\frac{t_{hc}}{D_{hc}}\right)^{0.0323}\left(\frac{t_{hc}D_{hc}}{S^2}\right)^{0.2881} \tag{21}$$

where $R^2 = 0.9498$.

7. Conclusion

A material point internal-structure model of the honeycomb panel is developed for the analysis of shielding capability for high-velocity impact. All the components of the panel, including the front facesheet, the rear facesheet and the cell walls of the honeycomb structure, are discretized with points. The impact process is simulated with material point method. Local point refinement is used for the case where the impact area is not limited in one cell. The internal-structure model is validated with several impact experiments and the empirical formulae.

Then morphologies of the impacted holes and the channeling effect are investigated for different projectile masses and impact velocities. The shape of the hole on the front facesheet is more close to a circle than that of the hole on the rear facesheet, which can be attributed to less influences from the honeycomb core. A measurement method by averaging the hole sizes of every 60° is developped for the hole on the rear facesheet. The hole diameter of the front facesheet is influenced much more by the projectile size other than the projectile speed. The equivalent hole diameter of the rear facesheet, however, shows relevance to both the impact velocity and the projectile size. Larger impact velocity leads to larger debris dispersion range, which suggests that the honeycomb sandwich panel may be more effective for shielding higher velocity impacts. Larger projectile is also found to result in larger channel taper.

The internal structure parameters are varied to investigate their influences on the hole dimensions and the channeling effect. The channeling effect decreases as the cell size increases, the thickness of the cell wall decreases, and the thickness of the whole honeycomb core decreases. Three empirical equations with respect to impact mass, impact velocity and internal structure parameters are presented for the hole diameters and the channel taper based on the computational results and the dimensional analysis.

The particle property of material point method provides fast and easy development of complicated internal-structure model as well as strong capability to capture the details in high-velocity impact process. Internal-structure-based investigation of shielding high-velocity impact with other new and complex materials will be the future work.

References

[1] Sennett RE, Lathrop BL. Effects of hypervelocity impact on honeycomb structures. J Spacecr Rockets 1968;5(12):1496–7.
[2] Turner RJ, Taylor EA, McDonnell JAM, Stokes H, Marriott P, Wilkinson J, et al. Cost effective honeycomb and multi-layer insulation debris shields for unmanned spacecraft. Int J Impact Eng 2001;26(1–10):785–96.
[3] Frate DT, Nahra HK. Hypervelocity impact testing of nickel hydrogen battery cells. In: Space Programs and Technologies Conference; 1996. Huntsville, AL, USA: AIAA meeting papers, A9641250.
[4] Frost CL, Rodriguez PI. AXAF hypervelocity impact test results. In: Kaldeich-SchÜrmann Brigitte, editor. Proceedings of second European conference on space debris. Noordwijk, Netherlands: ESA Publications Division; 1997. p. 423–8.
[5] Schäfer F, Destefanis R, Ryan S, Riedel W, Lambert M. Hypervelocity impact testing of CFRP/Al honeycomb satellite structures. In: Danesy D, editor. Proceedings of 4th European conference on space debris. Noordwijk, Netherlands: ESA Publications Division; 2005. p. 407–12.
[6] Putzar R, Schäfer F, Lambert M. Vulnerability of spacecraft harnesses to hypervelocity impacts. Int J Impact Eng 2008;35(12):1728–34.
[7] Schonberg W, Schäfer F, Putzar R. Hypervelocity impact response of honeycomb sandwich panels. Acta Astronaut 2010;66(3–4):455–66.
[8] Taylor EA, Herbert MK, Vaughan BAM, McDonnell JAM. Hypervelocity impact on carbon fibre reinforced plastic/aluminium honeycomb: comparison with Whipple bumper shields. Int J Impact Eng 1999;23(1):883–93.
[9] Taylor EA, Glanville JP, Clegg RA, Turner RG. Hypervelocity impact on spacecraft honeycomb: hydrocode simulation and damage laws. Int J Impact Eng 2003;29(1–10):691–702.
[10] Ryan S, Schäfer F, Destefanis R, Lambert M. A ballistic limit equation for hypervelocity impacts on composite honeycomb sandwich panel satellite structures. Adv Space Res 2008a;41(7):1152–66.
[11] Schonberg WP, Schäfer F, Putzar R. Predicting the perforation response of honeycomb Sandwich panels using ballistic limit equations. J Spacecr Rockets 2009;46(5):976–81.
[12] Johnson GR. Numerical algorithms and material models for high-velocity impact computations. Int J Impact Eng 2011;38(6):456–72.
[13] Hallquist JO. LS-DYNA User's Manual. Livermore, CA, USA: Livermore Software Technology Corporation; 2003. p. 8.119–20.
[14] Ryan S, Schäfer F, Riedel W. Numerical simulation of hypervelocity impact on CFRP/Al HC SP spacecraft structures causing penetration and fragment ejection. Int J Impact Eng 2006;33(1–12):703–12.
[15] Sulsky D, Chen Z, Schreyer HL. A particle method for history-dependent materials. Comput Methods Appl Mech Eng 1994;118(1–2):179–96.
[16] Ma S, Zhang X, Qiu XM. Comparison study of MPM and SPH in modeling hypervelocity impact problems. Int J Impact Eng 2009;36(2):272–82.
[17] Sulsky D, Schreyer HL. Axisymmetric form of the material point method with applications to upsetting and Taylor impact problems. Comput Methods Appl Mech Eng 1996;139(1–4):409–29.
[18] Chen Z, Hu W, Shen L, Xin X, Brannon R. An evaluation of the MPM for simulating dynamic failure with damage diffusion. Eng Fract Mech 2002;69(17):1873–90.
[19] Shen L. A rate-dependent damage/decohesion model for simulating glass fragmentation under impact using the material point method. CMES – Comput Model Eng Sci 2009;49(1):23–45.
[20] Lian YP, Zhang X, Liu Y. An adaptive finite element material point method and its application in extreme deformation problems. Comput Methods Appl Mech Eng 2012;241–244:275–85.
[21] Huang P, Zhang X, Ma S, Wang HK. Shared memory OpenMP parallelization of explicit MPM and its application to hypervelocity impact. CMES – Comput Model Eng Sci 2008;38(2):119–47.
[22] Gong WW, Liu Y, Zhang X, Ma HL. Numerical investigation on dynamical response of aluminum foam subject to hypervelocity impact with material point method. CMES – Comput Model Eng Sci 2012;83(5):527–45.
[23] Liu Y, Wang HK, Zhang X. A multiscale framework for high-velocity impact process with combined material point method and molecular dynamics. Int J Mech Mater Des 2013;9(2):127–39.
[24] Liu P, Liu Y, Zhang X, Guan Y. Investigation on high-velocity impact of micron particles using material point method. Int J Impact Eng 2015;75:241–54.
[25] Johnson GR, Cook WH. A constitutive model and data for metals subjected to large strains, high strain rates and high temperatures. In: Proceedings of the 7th international symposium on ballistics, vol. 21. The Hague, Netherlands: International Ballistics Committee; 1983. p. 541–7.
[26] Nicholas T, Rajendran AM. Material characterization at high strain rates. In: Zukas JA, editor. High velocity impact dynamics. New York, USA: John Wiley & Sons, Inc; 1990. p. 127–296.
[27] Giacomuzzo C, Pavarin D, Francesconi A, Lambert M, Angrilli F. SPH evaluation of out-of-plane peak force transmitted during a hypervelocity impact. Int J Impact Eng 2008;35(12):1534–40.

[28] Poteet CC, Blosser ML. Improving metallic thermal protection system hypervelocity impact resistance through numerical simulations. J Spacecr Rockets 2004;41(2):221–31.
[29] Johnson GR, Cook WH. Fracture characteristics of three metals subjected to various strains, strain rates, temperatures and pressures. Eng Fract Mech 1985;21(1):31–48.
[30] Lee R, Osher J, Chau H, Gerassimenko M, Pomykal G, Speer R. The impact of flat, thin plates on aluminum targets in the 5-10 km/s velocity range. Int J Impact Eng 1993;14(1–4):451–65.
[31] Ma ZT, Zhang X, Huang P. An object-oriented MPM framework for simulation of large deformation and contact of numerous grains. CMES – Comput Model Eng Sci 2010;55(1):61–87.
[32] Zhang X, Lian YP, Liu Y, Zhou X. Material point method. Beijing: Tsinghua University Press; 2013. p. 38–102.
[33] Sulsky D, Zhou SJ, Schreyer HL. Application of a particle-in-cell method to solid mechanics. Comput Phys Commun 1995;87(1–2):236–52.
[34] Ryan S, Schäfer F, Guyot M, Hiermaier S, Lambert M. Characterizing the transient response of CFRP/Al HC spacecraft structures induced by space debris impact at hypervelocity. Int J Impact Eng 2008;35(12):1756–63.
[35] Ohtani K, Numata D, Kikuchi T, Sun M, Takayama K, Togami K. A study of hypervelocity impact on cryogenic materials. Int J Impact Eng 2006;33(1–12):555–65.
[36] Zhang YT, Zhang X, Liu Y. An alternated grid updating parallel algorithm for material point method using OpenMP. CMES – Comput Model Eng Sci 2010;69(2):143–65.
[37] Lesuer DR, Kay GJ, LeBlanc MM. Modeling large-strain, high-rate deformation in metals. In: Shapiro AB, editor. Third biennial tri-laboratory engineering Conference modeling and simulation. Pleasanton, CA, USA: Lawrence Livermore National Laboratory, UCRL-JC-134118; 1999.
[38] Maiden CJ, McMillan AR. An investigation of the protection afforded a spacecraft by a thin shield. AIAA J 1964;2(11):1992–8.